Atmospheric Environment 231 (2020) 117533

Contents lists available at ScienceDirect

Atmospheric Environment

journal homepage: http://www.elsevier.com/locate/atmosenv

Aerosol absorption over the Aegean Sea under northern summer winds

Georgia Methymaki [a,*], Elissavet Bossioli [a], John Kalogiros [b], Giorgos Kouvarakis [c], Nikolaos Mihalopoulos [b,c], Athanasios Nenes [d,e], Maria Tombrou [a]

[a] Department of Physics, National and Kapodistrian University of Athens, Athens, 15772, Greece
[b] Institute for Environmental Research and Sustainable Development, National Observatory of Athens, Athens, 15236, Greece
[c] Department of Chemistry, University of Crete, Heraklion, 700 13, Greece
[d] Laboratory of Atmospheric Processes and Their Impacts, School of Architecture, Civil and Environmental Engineering, École Polytechnique Fédérale de Lausanne, Lausanne, 1015, Switzerland
[e] Institute for Chemical Engineering Sciences, Foundation of Research and Technology Hellas, Patras, 26504, Greece

HIGHLIGHTS

- The forcing of BC, dust, and sea salt absorption under Etesians is estimated at 1.2, 0.1 and nearly zero W m^{-2}, accordingly.
- BC absorption reduces the SW↓ by 5.5 W m^{-2} near the surface and augments the LW↑ by 0.3 W m^{-2} at the TOA.
- BC absorption reduces the cloud water mixing ratio on average by 10% (semi-direct effect).
- BC absorption influences all physical and dynamical heating processes producing heating rates up to 0.2 K day^{-1}.
- The mean daily temperature increases by up to 0.8 K near the surface.

ARTICLE INFO

Keywords:
Aerosol absorption
Black carbon absorption
WRF-Chem
Direct effect
Semi-direct effect
heating rate
Mediterranean
Aerosol-radiation interaction

ABSTRACT

In this modelling study, the absorption influence on radiation, apart from scattering, is studied above the Aegean Sea (Eastern Mediterranean) under a typical warm 13-day period with northern winds, transporting polluted air masses. The simulated (WRF-Chem) forcing caused by the total absorption is estimated along with black carbon (BC), dust, and sea salt contributions, 1.3, 1.2, 0.1 and nearly zero W m^{-2}, accordingly. As dust and sea salt influence is negligible, the main focus is on BC. BC absorption reduces downward shortwave irradiance reaching the ground by up to 5.2 W m^{-2} and the upward part by up to 1.7 W m^{-2}. The downward and the upward longwave irradiances are augmented by up to 2.3 and 1.2 W m^{-2}, accordingly. Even though the cloud formation is not favoured during the study period, BC absorption reduces overall the cloud water mixing ratio by 10% (semi-direct effect). However, during specific days and over limited cloudy areas, the semi-direct effect reduces low level clouds up to 20% while in case of higher clouds the reduction reaches up to ~29%. In order to examine the physical mechanisms below semi-direct effect, all modelled heating rates are analysed. Radiation direct absorption increases the air temperature with a rate up to 0.2 K day^{-1}, with an exception inside the surface layer, where unexpectedly longwave cooling prevails. The heating of the surface layer is mainly attributed to the advection process, as more heated air masses are transported over the Aegean Sea.

1. Introduction

Atmospheric aerosols are the most uncertain driver of global climate change (IPCC et al., 2013). The particles scatter and absorb solar and terrestrial radiation (Angstrom, 1929; Coakley et al., 1983; Charlson et al., 1992; Ramanathan and Feng, 2009; Boucher et al., 2013), the so called direct effect. Through the aerosol absorption, the temperature, the atmospheric stability, and the near-cloud relative humidity are locally altered and consequently modify the cloudiness, well known as the semi-direct effect (Hansen et al., 1997; Ackerman et al., 2000; Jacobson, 2002). Concurrently, aerosols serve as cloud condensation or ice nuclei (indirect effect) (Gunn and Phillips, 1957; Twomey, 1972; Altaratz et al., 2014), thus indirectly cool the planet by increasing its albedo, the first indirect effect (Twomey, 1974, 1977), and differentiate

* Corresponding author.
E-mail address: gmethymaki@phys.uoa.gr (G. Methymaki).

https://doi.org/10.1016/j.atmosenv.2020.117533
Received 13 November 2019; Received in revised form 2 March 2020; Accepted 17 April 2020
Available online 22 April 2020
1352-2310/

the cloud cover, the lifetime of clouds, and the precipitation, the second indirect effect (Albrecht, 1989; Rosenfeld, 2000; Ackerman et al., 2004; Wilcox, 2012; Zhou et al., 2017; Gordon et al., 2018; Rao and Dey, 2020). Each aerosol or a combination of aerosols alters the radiation budget. This change is expressed by the term forcing and it is defined as the change in the net vertical irradiance at the tropopause caused by a particular constituent.

The Mediterranean region is an area affected by a high aerosol load owed to air masses carrying numerous and various aerosol types from Europe, Africa, and Asia (Lelieveld et al., 2002). Recent studies demonstrate that these aerosol mixtures are significant on the radiation budget and cloud properties (Bougiatioti et al., 2009, 2016), especially over the Eastern Mediterranean where the phenomenon is more pronounced (Mallet et al., 2013). The direct, semi-direct, and indirect effects and forcings in the Mediterranean basin have been studied applying multiple techniques and methods, such as ground-based (Stock et al., 2011), airborne, cruise (Gerber, 1979), and satellite measurements (Georgoulias et al., 2015; Sicard et al., 2016) along with radiative transfer, climate, and forecasting models (Balis et al., 2004; Barnaba et al., 2007; Highwood et al., 2007; Di Biagio et al., 2009; Perrone and Bergamo, 2011; Nabat et al., 2014; Kushta et al., 2014; Mishra et al., 2014; Meloni et al., 2015; Mallet et al., 2016; Kosmopoulos et al., 2017). Markowicz et al. (2002) found that the anthropogenic aerosols from European and North African megacities result in a significant reduction in incoming solar radiation in the region, by $\sim$ 18 W m^{-2}, while Valenzuela et al. (2017) concluded that biomass burning (BB) and fossil fuel black carbon (BC) in the Iberian Peninsula attribute to radiative forcing by +15 W m^{-2}. Dust aerosols from Africa and Arabia Peninsula alter locally the solar irradiance by up to $\sim$ −15 W m^{-2} and the terrestrial one by up to $\sim$ +5 W m^{-2} (Spyrou et al., 2013), whereas marine particles change the net shortwave by $\sim$ −0.6 W m^{-2} and the net longwave irradiance by $\sim$ +0.2 W m^{-2} at the earth's surface (Lundgren et al., 2013).

Most studies that examine the aerosol-cloud-radiation interactions consider that the aerosol absorption and scattering are functioning simultaneously. However, given the fact that some effects depend either on the light absorption (e.g. the semi-direct and the cloud absorption) or on the light scattering (e.g. first indirect effect) (Jacobson, 2002a, 2014), we consider that it is preferable for each optical property to be examined separately. A few studies exist that quantify the influence of absorption or scattering, separately. Jin et al. (2016) found that dust absorption in the Middle East traps $\sim$ 40 W m^{-2} in the atmosphere, overlaps the scattering's cooling ($\sim$−0.2 K day^{-1}) ending up to an overall heating ($\sim$+0.2 K day^{-1}). Due to crop burning in East China, Yao et al. (2017) found that the brown carbon direct forcing on shortwave radiation (−0.22 W m^{-2}) was a combined effect of the positive absorption forcing (+0.21 W m^{-2}) and a stronger negative scattering forcing (−0.43 W m^{-2}).

In this study, we examine the absorption impact, apart from scattering, on shortwave and longwave irradiances. We estimate the forcing to address the energy captured by absorption and we quantify the resulting heating rates throughout the atmosphere over the Aegean Sea (Eastern Mediterranean). Based on the thermodynamic equation, we investigate all the physical processes that contribute to local heating (semi-direct effect). The absorption is studied separately for each aerosol (BC, the main absorber, dust, a major absorber on longwave, sea salt, a minor absorber with pronounced concentration) and as a whole.

The mesoscale Weather Research and Forecasting model fully coupled with chemistry and aerosols (WRF-Chem) (Fast et al., 2006), which allows the division of the aerosol absorption from scattering, is implemented. We simulate a 13-day period in the summer of 2011, as airborne measurements inside the PBL are available (Aegean Pollution: Gaseous and Aerosol airborne Measurements (Aegean-GAME) campaign; Tombrou et al., 2015). Besides, this particular summer has been characterised as a typical one with regard to the aerosol burden for this region (Mishra et al., 2014), with consistent northerly winds, the "Etesian winds" (Tyrlis and Lelieveld, 2013). During this period mixed anthropogenic and BB polluted air masses from eastern and central Europe were transported to the region (Tombrou et al., 2015; Athanasopoulou et al., 2015; Bossioli et al., 2016), while sea salt production, triggered by the strong northern winds, induced pronounced sea salt concentrations in the atmosphere. Although the Etesian outbreaks are not characterised by high dust loads, we also investigate how their concentrations transported from the Middle East due to Anatolian thermal low (Tyrlis and Lelieveld, 2013) shape the absorption effect.

2. Methodology and data

2.1. Model set-up

The present study uses the WRF-Chem model (version 3.4.1). The simulations are performed by applying a 'two-way' nesting approach on three modelled domains: the parent domain (d01) extends over the broader area of Europe (20°N-80°N, 15°W-45°E) having a resolution of 0.5° x 0.5° (Fig. S1). The first nested domain (d02) extends over the area of Greece and Italy (not shown) with a resolution of 0.167° x 0.167° and the innermost one (d03) covers the extended area of Greece (Fig. 1) with 0.056° x 0.056° resolution. The atmosphere is divided into 35 full vertical sigma levels; the first level is placed at approximately 10 m above ground level, while the isobar of 50 hPa comprises the simulated top of the model. Input data for the initial, lateral, and boundary conditions have been obtained from the National Centers for Environmental Prediction (NCEP) operational Global Final (FNL) Analyses, along with NOAA high-resolution (0.083° x 0.083°) Sea Surface Temperature (SST) Analysis Product. The gas phase chemistry is simulated by the RADM2 mechanism (Stockwell et al., 1990), while for the aerosols the Modal Aerosol Dynamics Model for Europe (MADE; Ackermann et al., 1998) for inorganic species and the Secondary Organic Aerosol Model (SORGAM; Schell et al., 2001) for secondary organic aerosols are used. The RADM2-MADE/SORGAM is used as it is found to have the smaller bias of BC concentration in an intercomparison study for the Eastern Mediterranean (Georgiou et al., 2018). Our set up is quite similar to the one presented by Bossioli et al. (2016). However, in order to meet our objectives in this study we consider the RRTMG radiation scheme (instead of RRTM and Goddard) and we activate the direct effect. We have only considered the direct aerosol-radiation interactions (not the indirect ones), as our goal is to study the semi-direct effect (Jacobson, 2012).

The Rapid Radiation Transfer Model for Global (RRTMG) scheme (Iacono et al., 2008) is used, as it is the only scheme that takes into account the direct aerosol radiation interaction both on the shortwave and longwave irradiances. In an intercomparison study over the area and period of interest, the RRTMG scheme turned out to be the most accurate on shortwave band among those that process the aerosols direct effect (Methymaki et al., 2018). This scheme utilises the correlated-k approach to calculate the fluxes and the heating rates. Fluxes are calculated over 14 spectral bands in shortwave, spanning from 0.2 to 12.2 μm and 16 bands in the longwave, from 3.08 to 1000 μm. Subgrid-scale cloud variability is considered incorporating the Monte Carlo independent column approximation (McICA) method (Barker et al., 2003; Pincus et al., 2003) with the optical properties of water and ice clouds calculated for each spectral band.

Moreover, for the needs of this study, we extract the irradiances and the heating rates of the thermodynamic equation in every model level. The heating rates refer to the physical schemes, radiation (absorbed, scattered, and emitted), PBL (vertical diffusion and mixing), cumulus (vertical subgrid scale convective fluxes), and microphysics (latent heat) and to the dynamical schemes (horizontal diffusion and advection). The refractive index of BC follows Bond and Bergstrom (2006) study. All aerosol mixtures are considered internally mixed and the volume average refractive index mixing rule is applied based on the chemical composition.

The study period, from 28-08-2011 to 09-09-2011, is mainly

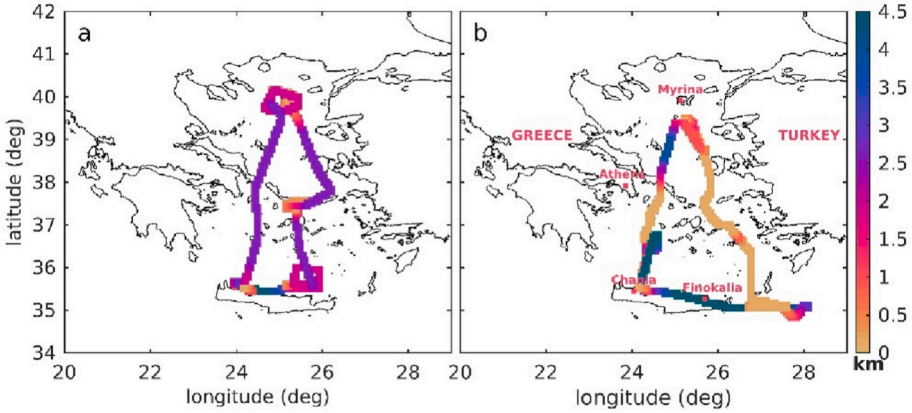

Fig. 1. Flight-track of a) b637 flight on 01-09-2011 and b) b643 flight on 07-09-2011. Colour scale depicts height. (For interpretation of the references to color in this figure legend, the reader is referred to the Web version of this article.)

designated by the available airborne measurements from the Aegean-GAME campaign (31-08-2011 to 07-09-2011, Bezantakos et al., 2013; Tombrou et al., 2015). Although the Aegean-GAME campaign starts on 31-08, the study period begins three days earlier, on 28-08, so that days characterised as Etesians (Tyrlis and Lelieveld, 2013) to be also considered. The study period is splitted into three shorter subperiods for meteorology with two spin up days for each one. The simulations start two days earlier, on 26-08-2011, so that the chemical and aerosol pollution can be advected to the innermost domain through large-scale transport. Only for the first simulated day (26-08-2011) idealised profiles, based on climatological data from the NOAA Aeronomy Lab Regional Oxidant Model (NALROM) (McKeen et al., 1991), are employed. For the next days, the chemistry runs continuously.

2.2. Emissions

The anthropogenic emission inventory from the European Monitoring and Evaluation Programme (EMEP) with emissions from ships and volcanoes for the reference year 2010 is used for domain d01 in a spatial resolution 0.5° x 0.5° and projected to domain d02, while the national emission inventory (0.056° x 0.056° resolution) is applied in the domain d03 (Tombrou et al., 2009). Sea-salt and dust emissions are generated on-line using the MOSAIC and MADE/SORGAM emissions. Biogenic emissions are also calculated on-line, based on the algorithm provided by Guenther et al. (1993), whereas daily actual patterns of BB emissions have been calculated off-line for the domains d01 and d02, based on the total particulate matter BB emission inventory (resolution of 0.1° × 0.1°) of the FMI FAS system (Sofiev et al., 2009). Anthropogenic and BB emissions for BC in d01 are depicted in Fig. S1, whereas a more detailed view of the emissions applied can be found in Bossioli et al. (2016).

Given the meteorological conditions (northern winds) during the examined period, the transported air masses are mainly burdened by anthropogenic and BB emissions, therefore, the BC appears to be the most significant absorber. Comparing the BC concentration from the first complete simulation (AA_{old} run), which followed all the details described above and in section 2.4, with airborne measurements from Aegean Pollution: Gaseous and Aerosol airborne Measurements (Aegean-GAME) campaign and data from the Finokalia station, it became apparent that BC is seriously underestimated by 77% and 66%, accordingly (Table 1). These percentages are not acceptable based on Emery et al. (2017) thus, after multiple sensitivity runs, in order to approach the measured BC load, the BC emissions (from BB and anthropogenic sources) are doubled in all simulations. Finally, the underestimation is reduced to 54% and 32%, accordingly (Table 1). Although the comparison with the airborne data is still out of the criteria, we considered it as reasonable as the normalised mean error (NME) is inside the proposed criteria. Larger deviations can be explained by the numerous close to zero values of BC concentration that are measured at high altitudes and increase the fraction of the normalised mean bias (NMB) artificially.

Table 1
Statistical evaluation of AA with the available datasets: airborne (31-08-2011 to 07-09-2011) and Finokalia data (28-08-2011 to 09-09-2011). The evaluation of BC concentration is presented for the base AA simulation (and the AA_{old} run with initial BC emissions). The measured scattering coefficient includes both particles and Rayleigh scattering.

Aegean-GAME	Absorption Coefficient (565 nm) (Mm^{-1})	BC Concentration ($\mu g\ m^{-3}$)	Downward Shortwave Radiation ($W\ m^{-2}$)	Upward Shortwave Radiation ($W\ m^{-2}$)
Mean Observed Value	2.96	0.30	783	79.8
Mean Bias	−1.39	−0.15(-0.22)	34.3	25.6
Normalised Mean Bias	−0.49	−0.54(-0.77)	0.05	0.38
Normalised Mean Error	0.68	0.68(0.79)	0.08	0.47
Finokalia	Absorption Coefficient (880 nm) (Mm^{-1})	BC Concentration ($\mu g\ m^{-3}$)	Downward Shortwave Radiation ($W\ m^{-2}$)	Scattering Coefficient (532 nm) (Mm^{-1})
Mean Observed Value	2.77	0.58	455	49.0
Mean Bias	−0.03	−0.19(-0.38)	30.3	−14.1
Normalised Mean Bias	0.00	−0.32(-0.66)	0.07	−0.29
Normalised Mean Error	0.47	0.45(0.66)	0.16	0.44

2.3. Simulations and off-line calculations

WRF-Chem ran five times, all with doubled BC emissions: i) All the aerosols Absorb (AA), as the base run, ii) none aerosol absorbs (WoA), and the cases where iii) BC (WoBC), iv) dust (WoDust), and v) sea salt (WoSS) do not absorb. A specific aerosol is not allowed to absorb by setting the imaginary part of the refractive index to zero. The absorption for each aerosol is studied via the difference of 2 simulations: the basic simulation AA, where all aerosols have the ability to absorb, and the simulation where the specific aerosol is not allowed to absorb (e.g. WoBC). This approach eliminates other aerosols absorption. In addition,

a sensitivity simulation is realised, where BC neither absorbs nor scatters radiation ($WoBC_{abs+scatt}$) in order, compared with AA, to deduce the total BC radiative impact (scattering and absorption in synergy).

In order to calculate the modelled absorption coefficient at 880 nm and 565 nm and evaluate model results (for the AA simulation), we first calculate the single scattering albedo and the extinction coefficient at the desired wavelengths. More specifically, we compute the single scattering albedo and the extinction coefficient at the desired wavelengths (using their simulated values at the default wavelengths (300, 400, 600, and 999 nm)) by applying linear interpolation for single scattering albedo and the Angstrom exponent for the extinction coefficient, following RRTMG structure. Then, the basic formula of single scattering albedo (ratio of scattering coefficient to extinction coefficient) is used to calculate the scattering coefficient and finally the absorption coefficient.

The direct forcing of each aerosol is calculated by the formula,

$$\sum_{i=1}^{N} \frac{NET_i^{AA} - NET_i^{WoA}}{N} \quad (1)$$

where N is the number of hours, NET^{AA} the hourly net irradiance in the AA simulation, and NET^{WoA} the net irradiance in the WoA, WoBC, WoDust, or WoSS scenarios. Also, NET is given by the formula,

$$NET = SW\downarrow + LW\downarrow - SW\uparrow - LW\uparrow \quad (2)$$

where SW↓ the downward shortwave irradiance, LW↓ the downward longwave irradiance, SW↑ the upward shortwave irradiance, and LW↑ the upward longwave irradiance at the tropopause (~15 km) which is calculated according to the World Meteorological Organization definition. The calculation was performed for all days during the selected period. The term forcing is used despite the requirements in the proposed definition by IPCC, just to address the energy (in W m^{-2}) captured by each aerosol separately or the total absorption inside the troposphere.

2.4. Measurements

The available datasets come from the Aegean-GAME campaign (31-08 to 07-09, Bezantakos et al., 2013; Tombrou et al., 2015) and from the Finokalia surface station. Measurements from Finokalia cover all the study period (28-08 to 09-09). The observations from the UK Facility for Airborne Atmospheric Measurements (FAAM) BAe-146 research aircraft (http://www.faam.ac.uk) cover the whole Aegean, inside and above the PBL (up to 4.5 km). In all flights, the aircraft took off from Chania airport on Crete and continued eastward before turning northward up to the northern Aegean Sea or to the northern coasts of Turkey. The paths of two flights above the Aegean are presented in Fig. 1. The airborne measurements are supported by hourly observations made at the Finokalia ground station (http://finokalia.chemistry.uoc.gr/) located on Crete (35° 20′ N, 25° 40’ E, at 250 m a.s.l.).

The statistics of WRF simulations against the airborne meteorological (temperature, wind speed, and relative humidity) and chemical (O_3, CO, $SO4^{2-}$, $NH4^{+}$, OM, BC) parameters are extensively discussed in Dandou et al. (2017) and Bossioli et al. (2016). In this study we focus on the radiation related parameters. Therefore, the measured airborne variables considered are a) the downward shortwave and upward shortwave irradiances measured using Eppley Pyranometer instruments on top and beneath the aircraft, respectively, with corrections for pitch and non-idealities (with sampling frequency of 0.01 Hz), b) the aerosol absorption coefficients at 565 nm measured with a Radiance Research Particle Soot Absorption Photometer (with sampling frequency of 0.01 Hz), and the estimated BC concentrations at aircraft ambient conditions, following the corrections described in Tombrou et al. (2015). The measured ground variables at Finokalia station are the hourly a) downward shortwave irradiance, measured by the CM3 Pyranometer by Campbell Scientific, INC., b) the BC concentration using the AE22 Magee Aethalometer at 880 nm and through it the aerosol absorption coefficients at 880 nm, following Zanatta et al. (2016), and c) the scattering coefficient at 532 nm by the monowavelength portable integrating nephelometer (M903, Radiance Research, Seattle, USA). Driven by the available measurements, we calculate the modelled absorption coefficient at 880 nm and 565 nm (section 2.3).

3. Results

During the study period, northern winds prevailed and according to simulations the ratio of $PM_{2.5}$ to PM_{10} mass concentrations is on average 0.5. In section 3.1 we present the statistical analysis of the modelled values against airborne and surface observations, while in sections 3.2 we analyse the days which show interesting features regarding the aerosols; days with elevated coarse aerosols and days with elevated concentrations of the fine fraction. In section 3.3 we present the direct forcing and effect due to the total absorption as well as to each aerosol absorption separately (BC, sea salt, dust) at the tropopause. In section 3.4 we present the BC absorption impact on temperature, on clouds (semi-direct effect), and on irradiances (direct absorption effect). On section 3.5 we explain how BC absorption influences the heating rates that produce the temperature rise and create the semi-direct effect.

3.1. Statistical evaluation

The comparison of AA simulation results with the airborne measurements (Table 1) shows that BC concentrations are underestimated by 0.15 μg m^{-3} (NMB: -54%) and absorption coefficient by 1.39 Mm^{-1} (NMB: -49%). Similarly, the comparison with Finokalia data (Table 1) shows underestimation of BC concentration by 0.19 μg m^{-3} (NMB: -32%), absorption by 0.03 Mm^{-1} (NMB: ~0%), and scattering coefficient by 14.10 Mm^{-1} (NMB: -29%) for the whole period.

The downward shortwave irradiance is well simulated; the mean deviation is +30.3 W m^{-2} (NMB: +7%) at the Finokalia station and +34.3 W m^{-2} (NMB: +5%) during the whole period of the Aegean-GAME (Table 1). These differences are mainly attributed to the aerosols underestimation (Methymaki et al., 2018) and the failure of the model to forecast accurately the existing clouds (Zempila et al., 2016). Although the overestimation of the downward shortwave irradiance is rather small, it initiates an overestimation of the upward shortwave irradiance, on average by 25.6 W m^{-2} (NMB: +38%) (Table 1). This is also related to the underestimation of scattering coefficient (NMB: -29% at Finokalia).

3.2. Case studies, 28-08, 01-09, and 07-09 of 2011

In Fig. 2, the simulated spatial distribution of aerosol total columnar masses of BC, dust, sea salt, and PM10 are presented over the greater Mediterranean region for the selected days; 28-08 mainly for dust and sea salt, 01-09 mainly for BC and 07-09 for the three types of aerosols. For the analysis of the case studies, the mean daily vertical profiles of each aerosol type above the Aegean Sea (refers to the area covered by the sea in Fig. S2) together with those of temperature, water vapour, cloud water mixing ratio, and wind speed are also presented for each day of the period considered (Fig. 3).

28-08 is an Etesian day with intense north-eastern wind (Fig. 3.2d). BC concentrations are very low throughout the column (Fig. 3.1a). Also, the highest dust concentration (~15 μg m^{-3}) located below 2 km is simulated this day (Fig. 3.1b). The dust particles are transported from the Middle East due to the cyclonic formation above Turkey (Fig. 2.1b). Similar events, but with higher concentrations, are discussed in Dayan et al. (1991) and usually last 1–2 days. In our study, the duration of the event is 2 days; on 29-08 the transport continues and dust concentration exceeds 10 μg m^{-3}. At the same time, the strong wind generates sea-salt aerosols and the concentration exceeds 15 μg m^{-3} (Fig. 3.1c). Therefore, PM_{10} concentration maximises on 28-08 (Fig. 3.1d).

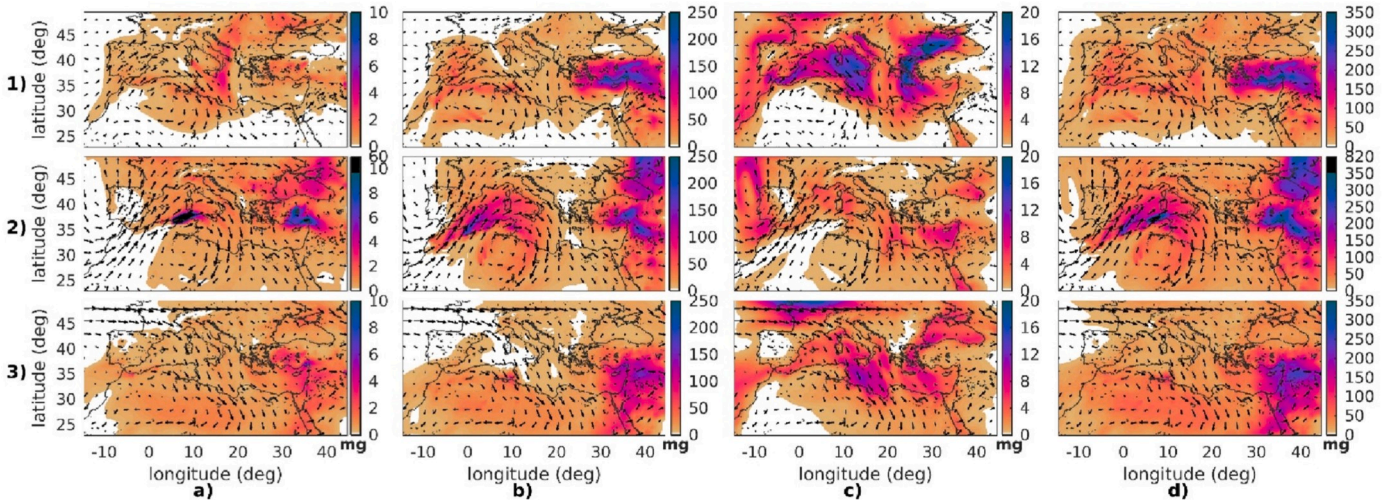

Fig. 2. Spatial horizontal patterns of total aerosol columnar mass per m^2 of: a) BC, b) dust, c) sea salt, and d) PM10 on 1) 28-08, 2) 01-09, and 3) 07-09, as simulated by AA. Wind direction is presented at ~2.5 km.

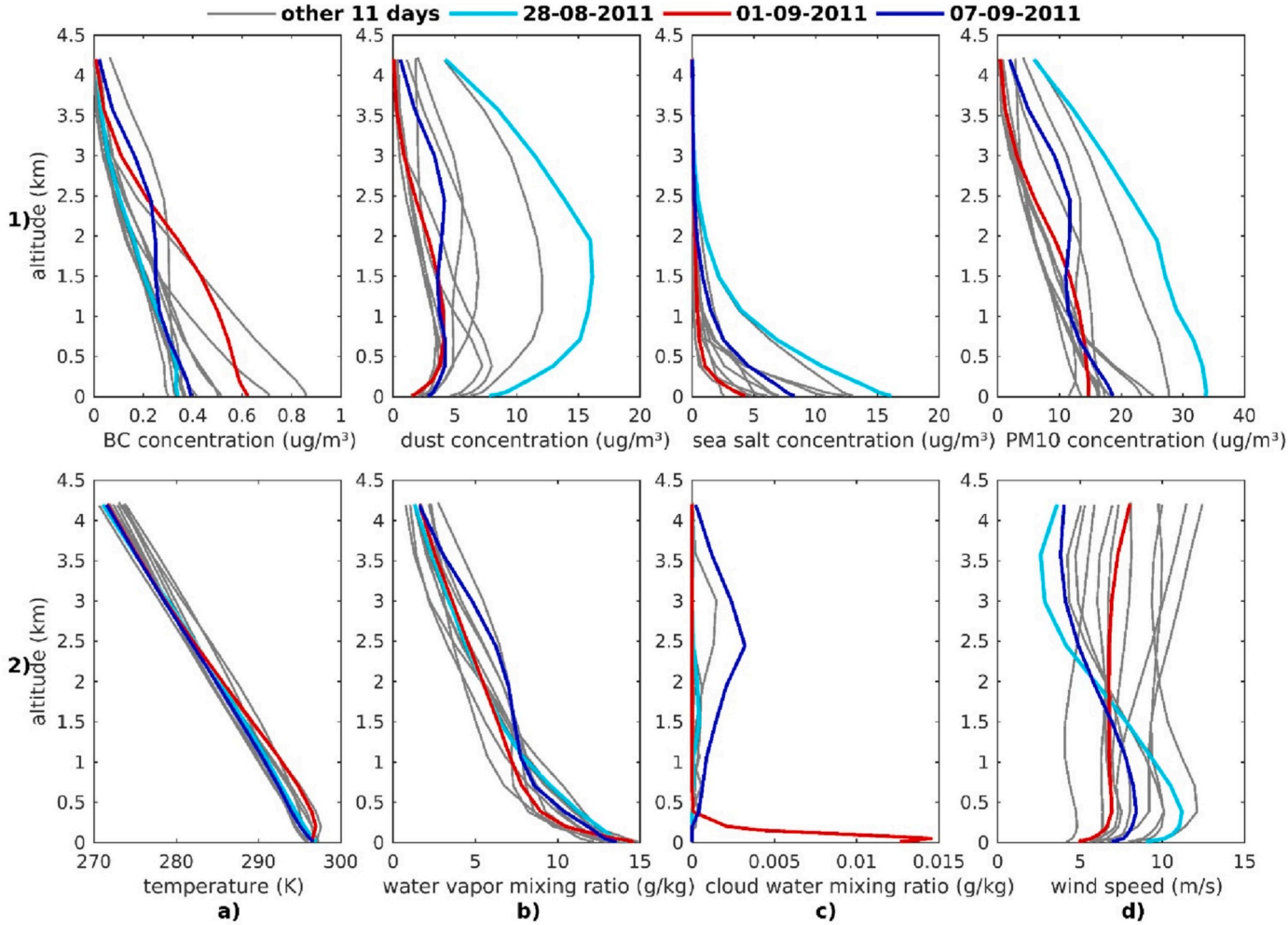

Fig. 3. Mean spatial (area covered by the sea, in Fig. S2) daily vertical profiles of: 1a) BC, 1b) dust, 1c) sea salt, 1d) PM10 concentration, 2a) temperature, 2b) water vapour and 2c) cloud water mixing ratio, and 2d) wind, as simulated by AA. The selected days are presented with colored lines (28-09, cyan; 01-09, red; 07-09, blue) and all other days with grey lines. (For interpretation of the references to color in this figure legend, the reader is referred to the Web version of this article.)

On 01-09 and 07-09, BC concentrations above the sea (Fig. 3.1a) retain the same amounts, or even higher, as those on land (Fig. S2a), despite the fact that they are further away from the emission sources, as the mixing of air masses transported over the sea is negligible. On 01-09, lower wind speeds prevail (Fig. 3.2d), which favours the accumulation of BC concentrations inside the PBL (Fig. 3.1a). The daily mean

horizontal distribution of BC columnar mass (Fig. S2.2a) shows that in the west Aegean the load is mainly due to local emissions, while in the east Aegean is mainly transported from Turkey along with BB aerosols (Fig. S6 in Bossioli et al., 2016). Meanwhile, low concentration of dust, sea salt, and PM_{10} are depicted in the area of interest (Fig. 3.1b,1c and 1d). During this day, higher cloud water mixing ratio values appear close to the sea (Fig. 3.2c).

The 07-09 is an Etesian day with high wind speed (although lower than on 28-08, at lower levels) that is significantly reduced at higher levels (Fig. 3.2d) favouring medium-range transport which augments the concentrations above the PBL, as extensively discussed by Tombrou et al. (2015). BC concentrations are lower than those on the 01-09 (Fig. 3.1a), however, they exhibit an elevated local maximum at ~2.5 km due to BB emissions transported to the area by the north-western flow (Bossioli et al., 2016). Low concentrations of dust and PM_{10} are calculated near the surface (Fig. 3.1b, d), but they increase at ~2.5 km in both profiles. Despite the fact that the dust load is small, this vertical structure corresponds to African dust transport (Flaounas et al., 2017). The anticyclone in the west Mediterranean during the previous days (as in Fig. 2.1b) carries dust particles west of Greece and the north-western flow on the 07-09 transports them to the Aegean Sea (Fig. 2.2b). Sea-salt is also enhanced (up to 8 μg m^{-3}) during this day. Therefore, dust and sea-salt are examined on 28-08 and 07-09 and BC on 01-09 and 07-09.

3.3. Direct absorption forcing and effect

Table 2 shows the direct forcing due to the total absorption as well as to each aerosol separately (BC, sea salt, dust) at the tropopause under all sky and cloud-free conditions for the total area (sea and land) in Fig. S2. Similarly, the direct effect on the downward shortwave and the upward longwave irradiances near the surface (at ~10 m) and at the top of the model are presented, accordingly. The results are provided during the whole period and for the selected days.

The mean absorbed irradiance by the total aerosol load for the whole period is found 1.3 W m^{-2} under all sky, most of which is due to BC (1.2 W m^{-2}, Table 2). Under clear sky conditions, the amounts do not differ significantly (1.2 and 1.1 W m^{-2}, correspondingly) as expected given the prevailing cloudless atmospheric conditions. The dust absorption forcing is insignificant, mainly due to its small overall concentrations. It only reaches up to 0.1 W m^{-2}, when transported from Middle East. The sea salt much lower absorptivity on shortwave than on longwave spectrum (even lower than dust's) allows the negative net on longwave to determine the outcome (~−0.05 W m^{-2}). However, the estimated BC forcing attributed both to absorption and scattering ($WoBC_{abs+scatt}$) is substantially reduced (0.3 W m^{-2}), showing that scattering reduces BC forcing by 0.9 W m^{-2}.

Under all sky conditions, the absorption of BC reduces the downward shortwave radiation near the surface by 5.5 W m^{-2} while the overall reduction is about 5.9 W m^{-2} (in cloud-free hypothesis, the reductions become 6.1 W m^{-2} and 6.4 W m^{-2}, accordingly). When the highest dust and sea-salt concentrations occur (on 28-08), dust reduces the downward shortwave irradiance by 0.5 W m^{-2}, while the sea salt reduction remains very low. The total absorption effect on the upward longwave radiation at the top of the model is +0.2 W m^{-2} (0.1 W m^{-2}, cloud-free hypothesis), of BC is +0.3 W m^{-2} (0.2 W m^{-2}, cloud-free hypothesis) and it is almost unnoticeable for dust and sea salt. The dust effect on longwave is not significant since longwave effect is also influenced by temperature and water vapour changes, as discussed in the next section. The fact that the total absorption effect is smaller than the BC absorption effect on longwave spectrum is artificial and it is due to the small variations produced between the simulations.

The impact of each absorber on the shortwave, longwave, and the total net irradiance in selected levels is presented in Fig. 4 for the study period. The bars at 15.2 km (tropopause) correspond to the forcing under all sky conditions (Table 2). It is apparent that the shortwave irradiance dominates the net profile at all levels, apart from that at the surface which is relatively smaller due to the higher longwave effect. Below 2 km, the absorption prevents the radiation from penetrating to lower levels, as the concentrations accumulate mainly there. Above 2 km, radiation is eased to penetrate to the lower levels. Dust follows BC and total absorption's tendency with height but it has much lower impact. Sea salt influence on the total net irradiance is negligible.

Due to the small contribution of dust and sea salt to the absorption, the discussion, hereafter, focuses on the BC absorption. A more detailed analysis of the days on which BC is examined (01-09 and 07-09) can be found in Supplements (Section S2) along with their evaluation with the airborne and the surface measurements.

Table 2
The direct forcing of absorption at the tropopause under all and clear sky conditions for all absorbing aerosols, BC, dust, and sea salt over the entire area (sea and land) in Fig. S2. Similarly, the direct effect of absorption on the downward shortwave (near the surface) and upward longwave irradiance (top of the model). The results correspond to the whole period (bold) and speciated for total and BC absorption on 01-09 (italic) and 07-09 (regular) and for dust and sea salt absorption on 28-08 (italic) and 07-09 (regular). LV indicates low absolute values, but not zero ($0.01 \leq |LV| < 0.05$).

			whole period/*01-09*/07-09		**whole period/*28-08*/07-09**	
Forcing (W m^{-2})	**Level**	**Sky**	**Total Abs.**	**BC**	**Dust**	**Sea Salt**
	tropopause	all sky	**1.3**/*1.9*/1.8	**1.2**/*1.8*/2.0	**LV**/*0.1*/-0.3	**LV**/*LV*/LV
	tropopause	clear sky	**1.2**/*1.7*/1.1	**1.1**/*1.6*/1.0	**LV**/*0.1*/LV	**LV**/*LV*/LV
Effect (W m^{-2})	**Level**	**Sky**	**Total Abs.**	**BC**	**Dust**	**Sea Salt**
SW↓	surface	all sky	**−5.9**/*8.6*/-3.5	**−5.5**/*8.1*/-2.2	**−0.2**/*0.5*/-0.9	**−0.1**/LV/-0.1
	surface	clear sky	**−6.4**/*8.8*/-6.8	**−6.1**/*8.6*/-6.6	**−0.2**/*0.4*/-0.3	**−0.1**/LV/-0.2
LW↑	top	all sky	**0.2**/*0.1*/1.0	**0.3**/*0.2*/1.3	**0.0**/LV/0.1	**LV**/*0.0*/LV
	top	clear sky	**0.1**/*0.1*/0.2	**0.2**/*0.2*/0.3	**0.0**/*LV*/LV	**0.0**/*0.0*/LV

3.4. BC absorption impact

3.4.1. Temperature

Fig. 5.1 depicts the spatial mean of the daily vertical profiles of the BC absorption coefficient derived as the difference of the absorption coefficients between the AA and the WoBC simulations along with its influence on the variables that are involved in the semi-direct effect, namely the cloud water, temperature, and water vapour. For most of the days, the higher temperature increase is calculated inside the PBL, with values up to 0.3 K (Fig. 5.1b), while this effect is noticeable up to ~3 km. On 07-09 however, the mean daily temperature increases by up to 0.17 K and it is found in the elevated layer with the enhanced BC concentrations. In areas without clouds, the daily increase in temperature near the surface may even reach 0.8 K (on 01-09, Fig. S3.1b). Mishra et al. (2014) observed through different satellite data a much higher impact of aerosols on temperature (up to ~ 4 K) in the Eastern Mediterranean, in the summer of 2010. During their study however, the aerosol load was much higher (AOD at 550 nm equal to 0.58) compared to that on the present study (0.10 on 01-09 and 0.16 on 07-09). They also found, in agreement with our study, that the impact is larger at higher altitudes inside the PBL than close to the surface. Comparable local temperature increases at 2 m (~0.2–0.6 K) driven by BC were found in Eastern China during a heavily polluted event (1-week long) using WRF-Chem (Qiu et al., 2017).

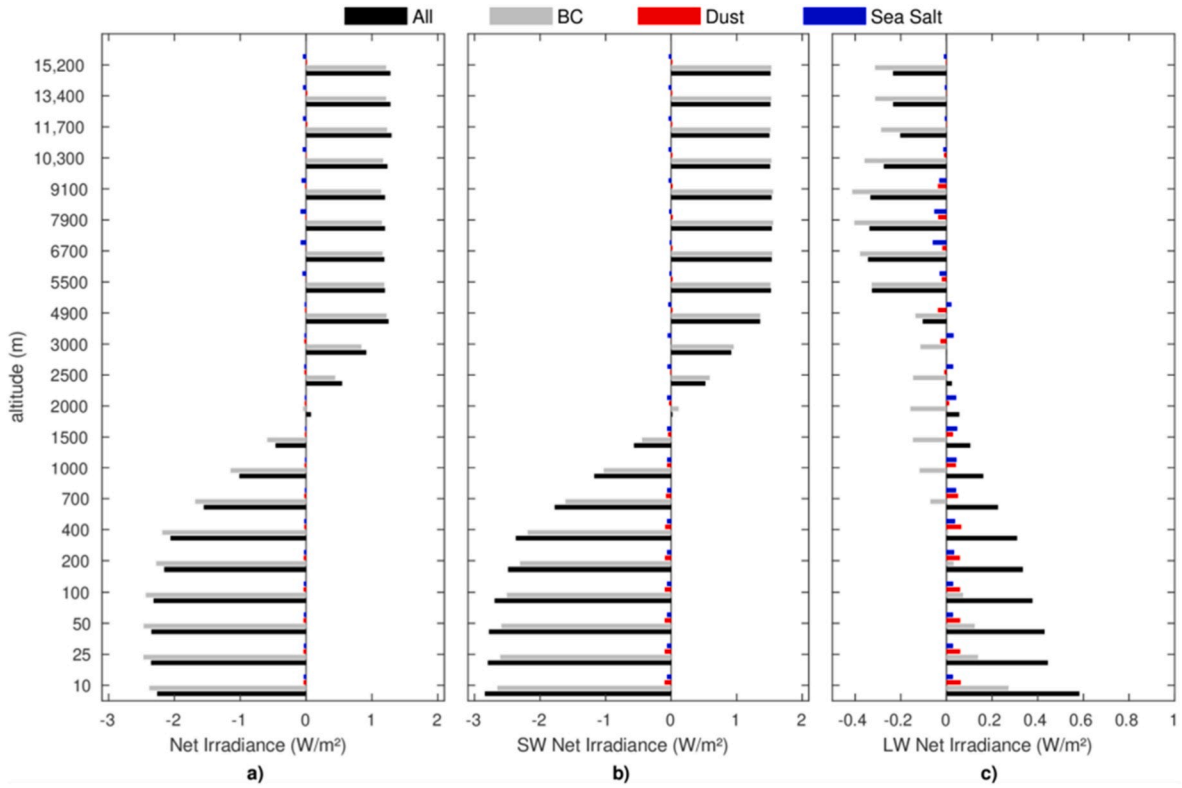

Fig. 4. a) Total, b) shortwave, and c) longwave net (↓-↑) irradiance differences; AA-WoA for total absorption (black), AA-WoBC for BC (grey), AA-WoDust for dust (red), and AA-WoSS for sea salt (blue) in selected model levels for the study period. (For interpretation of the references to color in this figure legend, the reader is referred to the Web version of this article.)

3.4.2. *Clouds (semi-direct effect)*

Even though the cloud formation is not favoured during this period, an overall reduction of cloud water mixing ratio by 10% is estimated. The rise in temperature favours the dissipation of existing clouds. Consequently, due to the evaporation of cloud droplets, the water vapour mixing ratio increases at about the same altitudes (Fig. 5.1c). We further examine two cloudy systems formed on 01-09 and 07-09. On 01-09 the cloud system is simulated near the surface, in the south Aegean (Fig. 3.2c, Fig. S4a) and coexists with high BC concentrations (Fig. 3.1a, Fig. S2.2a). The mean cloud water mixing ratio reaches up to 0.6 g kg^{-1} (Fig. S4a). On 07-09, the cloud system is formed in the northwest Aegean (Fig. S4b) in a cleaner environment (Fig. 3.1a), with a larger vertical development (200 m – 4 km) (Fig. 3.2c, Fig. S2.3a). The cloud water is up to 0.3 g kg^{-1} (Fig. S4b).

In order to further examine the BC semi-direct effect at these two areas, the mean profiles of cloud water mixing ratio, water vapour mixing ratio, relative humidity, vertical velocity, and temperature differences are presented in Fig. S5. For the mean profiles, we only consider the hours with clouds. On 01-09 the rise in temperature increases slightly with height in the surface layer (below 50 m) and does not affect the stability. However, the temperature increase enhances the production of water vapour (Fig. S3.1c) which stagnates near the surface due to the reduced wind speed (not shown) and, therefore, the cloudiness is augmented by 3%. In the following 100 m, the rise in temperature increases significantly with height and makes the column more stable reducing the cloud water by 20%. In the next 50 m, the temperature rise decreases with height and clouds develop. The overall reduction of clouds on 01-09 is ~14% (Fig. 5.1d). On 07-09, the alterations due to BC absorption do not follow the rise of temperature with height but the mean vertical wind reduction. Nevertheless, it is noted that there is a strong spatial variation of wind, where the intense topography seems to play a significant role, which is also depicted at the cloud pattern (Fig. S4b). This day, the mean reduction is 19%, while the maximum reduction (29%) is located at 2.5 km (Fig. 5.1d).

3.4.3. *Irradiances (absorption direct effect)*

For a complete view of the BC absorption direct effect, the mean spatial daily profiles of irradiance differences (AA-WoBC) are also presented in Fig. 5.2. On most days, the downward shortwave reduction under all sky conditions ranges from ~2.0 and up to ~5.2 W m^{-2} (near the surface), while it becomes less than 1.0 W m^{-2} at 4 km (Fig. 5.2a), following the absorption coefficient reduction with height (Fig. 5.1a). Further, in areas with high BC columnar mass (as on 01-09; Fig. S2.2a) the average daily reduction may even reach up to 15.0 W m^{-2} near the surface (Fig. S6.1b) under cloud-free conditions. The presence of clouds on 07-09 at ~2.5 km (Fig. 5.1d) reduces the irradiance impact at the surface by half (Fig. 5.2a). The sensitivity simulation $WoBC_{abs+scatt}$ shows that scattering further reduces the downward shortwave irradiance by 2.0 W m^{-2} on 01-09 and by 1.0 W m^{-2} on 07-09 near the sea (not shown). The total BC aerosol effect (synergy of absorption and scattering) in the downward shortwave irradiance for the whole period is −7.6 W m^{-2} (above the whole inner domain). Roger et al. (2006) based on aerosol measurements estimated BC effect equal to −15.6 W m^{-2} near Marseilles during 5 summer days under meteorological conditions more favourable to pollution events ($0.2 < AOD < 0.45$) than this study.

The upward shortwave irradiance depicts an absolute increase with height (Fig. 5.2b) as the reduction is accumulated upwards and has an opposite behaviour to that of the absorption coefficient (Fig. 5.1a). On most days it is reduced in the range of ~0.8–~1.7 W m^{-2} at ~4 km. The decreased cloud cover (Fig. 5.1d) augments the upward shortwave irradiance, as on 07-09, where the effect is more than doubled (Fig. 5.2b). Under cloud-free hypothesis, the irradiance is substantially reduced (e.g. by 1.5 and 1.0 W m^{-2} on 01-09 and 07-09, accordingly). These maximum absolute values remain almost constant at higher altitudes, since there is no further absorption. The spatial pattern of the

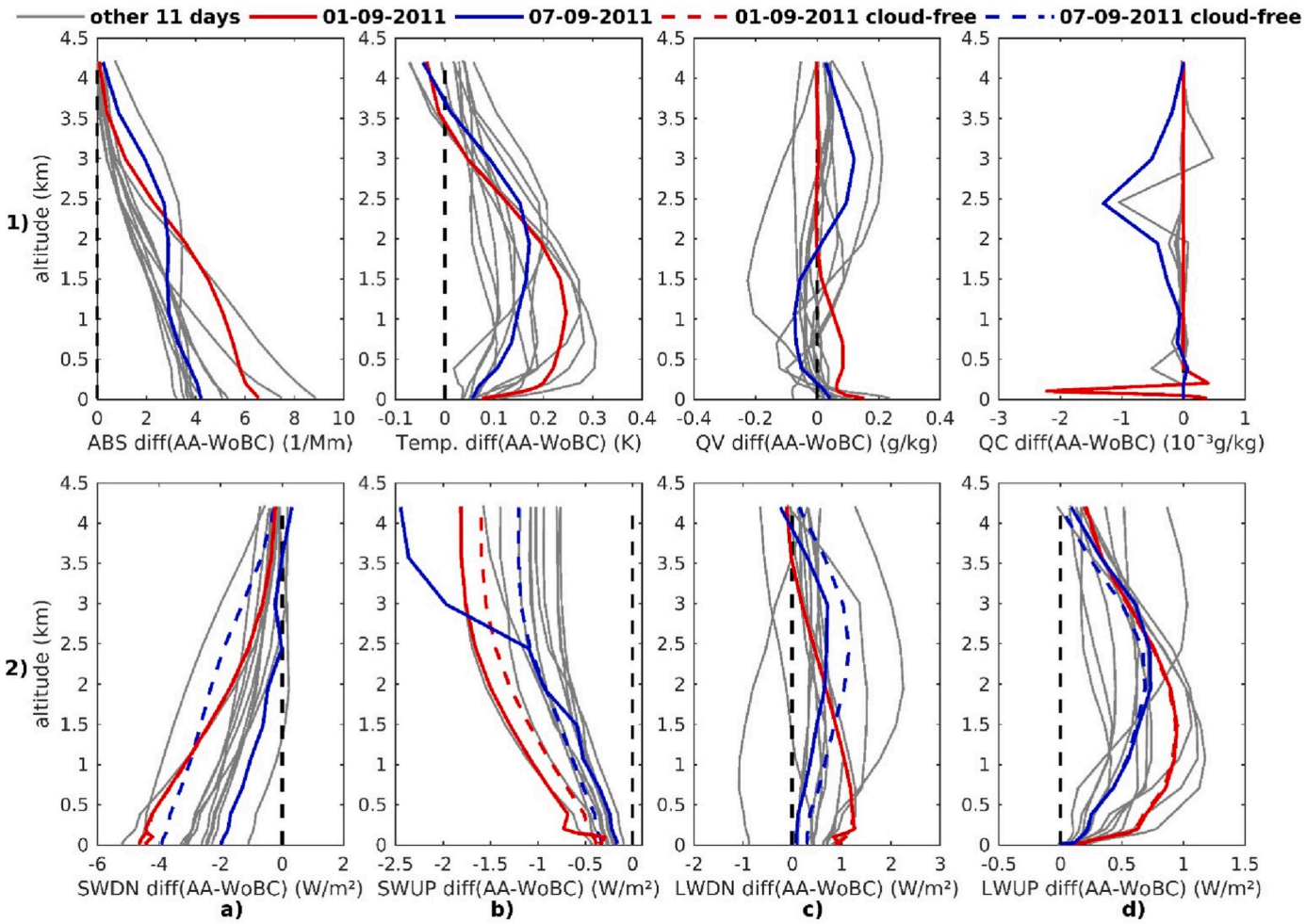

Fig. 5. As in Fig. 3, but for the difference (AA-WoBC) of: 1a) absorption coefficient at 565 nm, 1b) daily temperature, 1c) water vapour and 1d) cloud water mixing ratio, 2a) downward shortwave, 2b) upward shortwave, 2c) downward longwave, and 2d) upward longwave irradiance; on 01-09 (red), 07-09 (blue), and on all other days (grey). The solid lines are for all sky and the dashed lines for cloud-free hypothesis. (For interpretation of the references to color in this figure legend, the reader is referred to the Web version of this article.)

upward irradiance reduction follows the absorption one and reaches up to 8.0 W m^{-2} at the model top (e.g. on 01-09; Figs. S6.1d, S3.1a). The impact due to scattering becomes larger at the higher levels, almost eliminating the absorption effect, since the reflection of the downward irradiance accumulates with height (not shown). Therefore, the total BC effect reduces the upward shortwave irradiance by 1 W m^{-2} at TOA above the greater Greece area. Roger et al. (2006) found a 2.2 W m^{-2} reduction, correspondingly.

The mean spatial daily profiles of the downward longwave irradiance difference (Fig. 5.2c) depict a higher direct effect close to surface on 01-09 (~+1.0 W m^{-2}) than on 07-09 (nearly zero) due to the higher temperature increase during this day (0.2 K, Fig. 5.1b). This is also observed in the spatial pattern, where a mean daily effect near the surface reaches up to +4.0 W m^{-2} on 01-09 (Fig. S7.1b) and up to +2.0 W m^{-2} on 07-09 (Fig. S7.2b). The temperature impact on downward longwave irradiance is reduced when BC absorption is high, thus, the irradiance and the temperature difference profiles do not coincide; this is apparent on 01-09 (Fig. 5.1b and 5.2c). In addition, when both BC absorption and temperature increase are low, as on 07-09 (close to the surface, less than 4 Mm^{-1} and 0.1 K, Fig. 5.1a and b), water vapour difference becomes significant. On this day, the water vapour (Fig. 5.1c) traps the upward irradiance and reemits to both directions, increasing the downward irradiance by 1.0 W m^{-2} at 3 km where the maximum water vapour is located (Fig. 5.2c).

The upward longwave irradiance difference (Fig. 5.2d) follows the temperature difference (Fig. 5.1b). The maximum effect on 01-09 is + 1.0 W m^{-2} above the sea (higher above land), whereas on days with higher BC concentrations and therefore temperature increase, this maximum is exceeded. On 07-09, the increase approaches 0.8 W m^{-2}. The spatial distribution reveals that locally the mean daily increase reaches up to 1.0 W m^{-2} at the model top on the 01-09 (Fig. S7.1d), while it approaches 3.0 W m^{-2} on 07-09 (Fig. S7.2d) due to local temperature increase (Fig. S3.2b). The influence of water vapour on the upward irradiance is less visible than on the downward as water vapour absorbs the upward longwave irradiance and reemits to both directions.

3.5. Heating rates

The shortwave absorption has a positive impact on heating in all layers due to BC absoprtion. On 01-09, the mean vertical profile (above the sea) depicts a mean heating of 0.2 K day^{-1} close to the surface, which decreases with height (Fig. 6.1a) and follows the BC concentrations (Fig. 3.1a). Unlike most other days, on 07-09, the maximum heating is depicted above PBL, caused by BC transferred to these levels (Fig. 3.1a) and consequently enhances the temperature increase (Fig. 5.1b). On both days, the daily spatial distribution of heating rate close to the surface can reach locally 1.0 K day^{-1} (Figs. S8.1a,2a) responding to BC concentrations (Fig. S2a) and cloud differences (Fig. S3d). Ferrero et al. (2018) using one year experimental data (March 2015–March 2016) found that BC with ~1.25 μg m^{-3} mean concentration in summer and

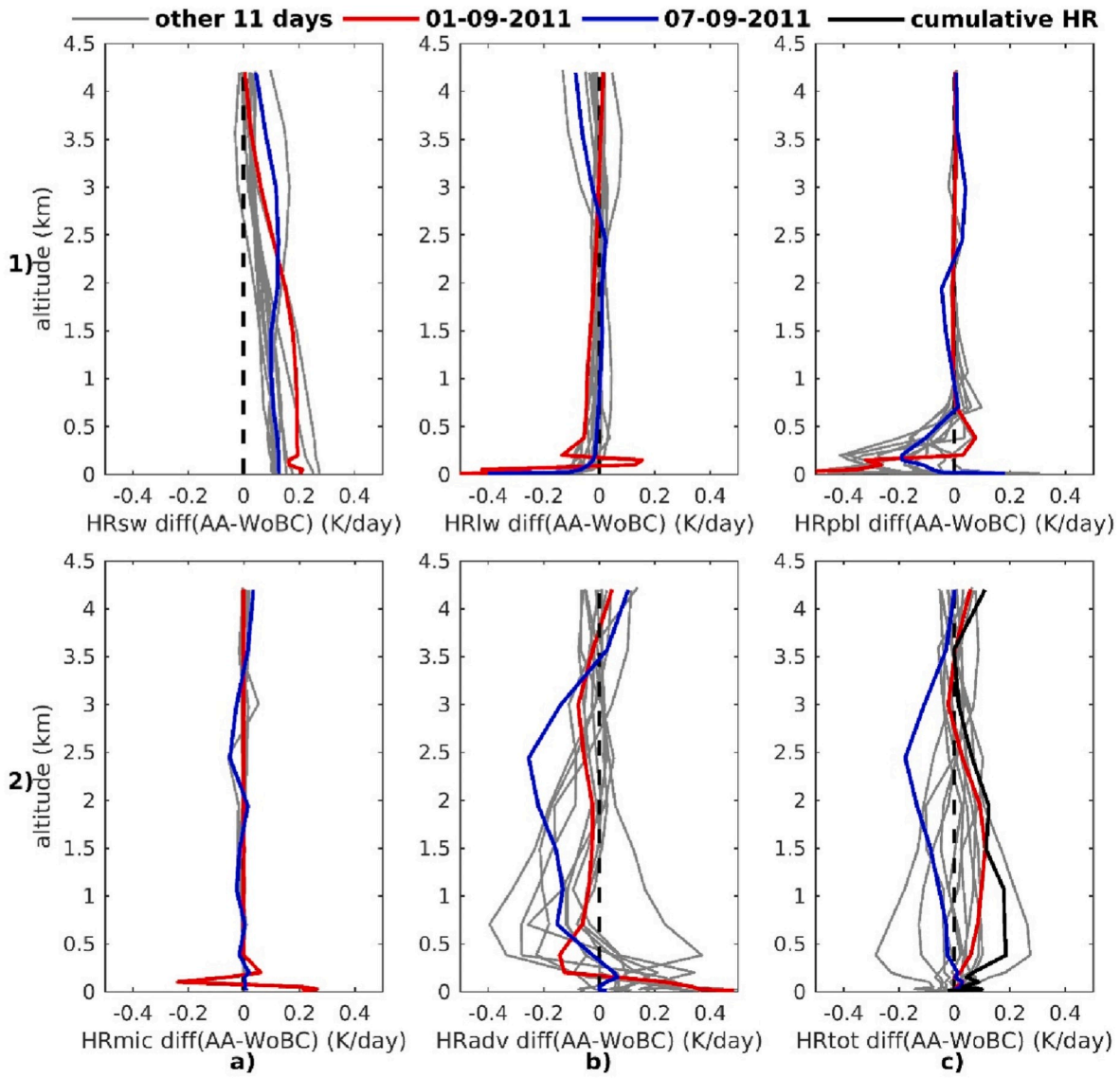

Fig. 6. As in Fig. 3, but for the heating rates difference (AA-WoBC) due to 1a) the shortwave and 1b) longwave radiation, 1c) the planetary boundary layer and 2a) microphysics processes, 2b) the advection, and 2c) the sum of all the physical processes on 01-09 (red), on 07-09 (blue) and on all the other days (grey) over the sea. The black line in 2c) is the cumulative heating rate. (For interpretation of the references to color in this figure legend, the reader is referred to the Web version of this article.)

~1.75 μg m^{-3} in autumn increases temperature in Milan at a mean rate of ~0.9 K day^{-1} and ~0.95 K day^{-1}, accordingly. Roger at al. (2006) found that shortwave heating rate exceeds 3.0 K day^{-1} for heavy anthropogenic pollution and 1.0 K day^{-1} for light pollution. Similarly, Saha et al., 2008 based on measurements during selected episodes (June 2006) found the heating rate at ~3.3 K day^{-1} due to polluted continental aerosols (AOD at ~ 0.30) transported at an urban coastal zone in South-eastern France.

As the BC concentration is in general reduced with height, it enables the upward longwave irradiance to escape to the free atmosphere and causes cooling inside the troposphere (Fig. 6.1b). In the atmospheric surface layer, the mean spatial daily rates range between −0.5 and −0.3 K day^{-1}. On 01-09 a heating rate of almost 0.2 K day^{-1} is triggered by cloud dissolution. Zhou and Savijärvi, 2014 introduced the effect of aerosols in a longwave radiation scheme by considering that the total aerosol mixture both scatters and absorbs radiation. They concluded to a cooling rate between 0.08 and 0.12 K day^{-1} for the reference clear-sky mid-latitude summer case of the International Comparison of Radiation Codes in Climate Models.

In general, the shortwave heating prevails over the longwave cooling in the atmosphere with a mean total rate up to 0.2 K day^{-1} (not shown). However, the impact of overall radiation near the surface is cooling (−0.3 K day^{-1}), as the longwave influence is dominant. Fig. 4a predisposed the negative radiation impact on heating in the surface layer; the net irradiance difference between the top and the base of this layer indicates energy release. However, at certain hours and days, when the shortwave irradiance is intense (about 900 W m^{-2}) and BC mean concentrations exceed 0.6 μg m^3, low heating (from 0.04 to 0.07 K day^{-1}) can occur in the surface. Mishra et al. (2014) found 0.45 K day^{-1} heating for polluted continental aerosols through a radiative transfer model, corresponding to a greater load (AOD: 0.58). The scattering influence was included in their study.

The remaining heating rates included in the thermodynamic equation are further analysed to explain their contribution on temperature increase. On most days, such as the 07-09, PBL mechanisms, mainly related to vertical diffusion and mixing, are enhanced by the BC absorption and contribute to the heating of the surface layer, up to 0.4 K day^{-1} (Fig. 6.1c), whereas just above and up to ~0.5 km they cause

cooling up to 0.4 K day^{-1}. On the contrary, on 01-09, the atmospheric surface layer is mainly affected by the cooler sea at a rate up to −0.5 K day^{-1}, as the increased stability due to the absorption (Fig. 5.1b) decouples this layer from the warmer upper ones. Horizontal diffusion has a small contribution to heating or cooling above the sea, up to 0.15 K day^{-1} that sharply tends to zero (not shown). Microphysics processes, through the latent heat, induces rates almost analogous to cloud water differences (Fig. 5.1d and 6.2a) but more pronounced in the surface (>0.2 K day^{-1}). The vertical (subgrid scale) convective fluxes computed by the cumulus scheme contribute slightly to the heating and cooling processes (not shown). The advection process appears to have a significant contribution to both cooling and heating throughout the atmosphere (Fig. 6.2b). On 01-09, the wind speed above the mainland of Greece transfers more heated air masses above the sea, producing a heating rate of ~0.5 K day^{-1}. On the other hand, on 07-09, the air masses with BC aerosols from northwest are less heated compared to those over the Aegean Sea thus, they induce cooling of more than 0.2 K day^{-1}.

Overall, on 01-09 (non-etesian day) the BC absorption adds to the temperature increase by up to 0.1 K day^{-1} (Fig. 6.2c) and thereby increases the atmospheric stability. In contrast, on 07-09 (etesian day), the physical processes tend to reduce temperature (Fig. 6.2c). Specifically, the air masses being mainly transported by the north-western flow are less heated by BC than the air over the study area, therefore they cause cooling. This is the reason why a relatively lower increase of temperature occurs during this day (Fig. 5.1b). During the whole studied period, the total daily sum of the heating rate due to BC absorption is less than 0.1 K day^{-1} at the atmospheric surface layer, but it increases (0.2 K day^{-1}) up to ~ 0.5 km mainly due to the advection and the radiation heating (black line in Fig. 6.2c). The increased values are maintained within the PBL (up to 2 km) as a result of the direct shortwave radiation absorption and determine the maximum temperature rise in these layers. A comparable study with WRF-Chem by Jin et al. (2016) considering dust absorption and scattering separately (but not the horizontal diffusion and the advection heating rates) found a mean heating rate of ~0.4 K day^{-1} for dust absorption in the Middle East in the summer of 2008 with 0.63 < AOD < 0.68.

4. Conclusions

At the Aegean Sea under a typical warm period with northern winds, where polluted air masses are transported from east and west, the simulated (WRF-Chem) total aerosol absorption leads to a tropopause forcing of 1.3 W m^{-2} and 1.2 W m^{-2}, under all sky and clear sky hypothesis, respectively. The main contributor is BC, trapping 1.2 W m^{-2} in the atmosphere under clear sky and 1.1 W m^{-2} under all sky conditions. Although the absorptivity of dust and sea salt on the longwave band is enhanced, their forcing is negligible under these synoptic patterns (0.1 W m^{-2} and nearly zero, accordingly).

The absorption of BC reduces downward shortwave irradiance reaching the ground (sea and land) by 5.5 W m^{-2} under all sky and 6.1 W m^{-2} under cloud-free conditions. The mean daily absolute values maximise above sea when BC burden is enhanced (up to 5.2 W m^{-2}), while the minimum ones are calculated during the Etesian days. The upward part of shortwave irradiance is also reduced by BC absorption, but increases its effect with height, up to 4 km, the level at which BC concentration tends to zero for the first time. The maximum reductions range between 0.8 and 1.7 W m^{-2}. The downward longwave radiation, influenced mainly by the increase of temperature, is augmented throughout the atmospheric column. The more pronounced influence is depicted in the levels where BC and/or water vapour are enhanced, varying from 0.3 to 2.3 W m^{-2}. The effect of the BC absorption on upward longwave irradiance is proportional to temperature increase and the maximum values (+0.4 - +1.2 W m^{-2}) are located between 0.7 and 2.5 km.

The differences on irradiances due to BC absorption influence the temperature and cloud formation. The most significant temperature increases are calculated inside PBL up to ~3 km, with spatial daily mean values reaching up to 0.3 K. In cloudless areas, the mean daily increase can reach up to 0.8 K near the surface. The increase further alters the cloud formation and the cloud water mixing ratio by ~ −10% in the cloudy layers. Low level clouds are reduced up to 20%; this change is mainly associated with temperature, thus, stability changes in the vertical. For higher clouds, the reduction reaches up to ~29% and is mainly associated with the strong spatial variation of wind and vertical wind reduction.

We further investigate how BC absorption influences the heating rates over the Aegean Sea that finally produce the temperature rise and create the semi-direct effect. It is found that BC absorption increases the temperature directly by the instant absorption of the radiation, and indirectly by the alterations it causes mainly to the advection, the vertical diffusion, and latent heating processes. At the layers above ~0.5 km, the cumulative heating (0.1–0.2 K day^{-1}) is mainly attributed to the absorption of shortwave radiation, as advection tends to bring colder air masses at those layers and the other physical processes contribution is negligible. On the other hand, between the 0.5 km and the atmospheric surface layer, the advection and shortwave radiation acts positively on the heating of the atmosphere where the vertical diffusion and mixing produce cooling in these layers with an overall small positive outcome. At the atmospheric surface layer, all physical processes, altered by BC absorption, act together to a different extent in order to heat or cool the layer, with a small total outcome (less than 0.1 K day^{-1}). Nevertheless, it is interesting to note that although the shortwave radiation heats the surface layer, longwave radiation cools it at a higher rate; therefore, total radiation direct absorption has a cooling tendency up to 0.2 K day^{-1} at the layer where the highest BC concentration is located.

Declaration of competing interest

The authors declare that they have no known competing financial interests or personal relationships that could have appeared to influence the work reported in this paper.

Acknowledgements

This research is co-financed by Greece and the European Union (European Social Fund- ESF) through the Operational Programme « Human Resources Development, Education and Lifelong Learning» in the context of the project “Strengthening Human Resources Research Potential via Doctorate Research” (MIS-5000432), implemented by the State Scholarships Foundation (IKY). Also, this work was supported by computational time granted from the National Infrastructures for Research and Technology S.A. (GRNET S.A.) in the National HPC facility - ARIS - under project ID pr005015”. This work is also supported by the EUFAR Integrating Activity (227159) funded by EC under FP7 and the UK Natural Environment Research Council [Grant Ref: NE/E018092/1]. Airborne data were obtained using the BAe-146-301 Atmospheric Research Aircraft (ARA) flown by Direct flight Ltd and managed by the Facility for Airborne Atmospheric Measurements (FAAM), which is a joint entity of NERC and the Met Office. We would like to acknowledge Prof. Steven Cavallo for sharing his knowledge regarding the tendencies of the thermodynamic equation of WRF-Chem model.

Appendix A. Supplementary data

Supplementary data to this article can be found online at https://doi.org/10.1016/j.atmosenv.2020.117533.

References

Ackerman, A.S., Toon, O.B., Stevens, D.E., Heymsfield, A.J., Ramanathan, V., Welton, E. J., 2000. Reduction of tropical cloudiness by soot. Science 288, 1042–1047. https://doi.org/10.1126/science.288.5468.1042.

Ackerman, A.S., Kirkpatrick, M.P., Stevens, D.E., Toon, O.B., 2004. The impact of humidity above stratiform clouds on indirect aerosol climate forcing. Nature 432, 1014–1017. https://doi.org/10.1038/nature03174.

Ackermann, I.J., Hass, H., Memmesheimer, M., Ebel, A., Binkowski, F.S., Shankar, U., 1998. Modal aerosol dynamics model for Europe: development and first applications, Atmos. Environ. Times 32, 2981–2999. https://doi.org/10.1016/S1352-2310(98)00006-5.

Albrecht, B.A., 1989. Aerosols, cloud microphysics, and fractional cloudiness. Science 245, 1227–1230. https://doi.org/10.1126/science.245.4923.1227.

Altaratz, O., Koren, I., Remer, L.A., Hirsch, E., 2014. Cloud invigoration by aerosols - coupling between microphysics and dynamics. Atmos. Res. 140, 38–60. https://doi.org/10.1016/j.atmosres.2014.01.009.

Angstrom, A., 1929. On the atmospheric transmission of sun radiation and on dust in the air. Geogr. Ann. Stockh. 11, 156–166. https://doi.org/10.2307/519399.

Athanasopoulou, E., Protonotariou, A.P., Bossioli, E., Dandou, A., Tombrou, M., Allan, J. D., Coe, H., Mihalopoulos, N., Kalogiros, J., Bacak, A., Sciare, J., Biskos, G., 2015. Aerosol chemistry above an extended archipelago of the eastern Mediterranean basin during strong northern winds. Atmos. Chem. Phys. 15, 8401–8421. https://doi.org/10.5194/acp-15-8401-2015.

Balis, D.S., Amiridis, V., Nickovic, S., Papayannis, A., Zerefos, C., 2004. Optical properties of Saharan dust layers as detected by a Raman lidar at Thessaloniki, Greece. Geophys. Res. Lett. 31, L13104. https://doi.org/10.1029/2004GL019881.

Barker, H.W., Stephens, G.L., Partain, P.T., Bergman, J.W., Bonnel, B., Campana, K., Clothiaux, E.E., Clough, S., Cusack, S., Delamere, J., Edwards, J., Evans, K.F., Fouquart, Y., Freidenreich, S., Galin, V., Hou, Y., Kato, S., Li, J., Mlawer, E., Morcrette, J.-J., O'Hirok, W., Raisanen, P., Ramaswamy, V., Ritter, B., Rozanov, E., Schlesinger, M., Shibata, K., Sporyshev, P., Sun, Z., Wendisch, M., Wood, N., Yang, F., 2003. Assessing 1D atmospheric solar radiative transfer models: Interpretation and handling of unresolved clouds. J. Clim 16, 2676–2699. https://doi.org/10.1175/1520-0442(2003)016<2676:ADASRT>2.0.CO;2.

Barnaba, F., Gobbi, G.P., De Leuuw, G., 2007. Aerosol stratification, optical properties and radiative forcing in Venice (Italy) during ADRIEX. Q. J. R. Meteorol. Soc. 133 (S1), 47–60. https://doi.org/10.1002/qj.91.

Bezantakos, S., Barmpounis, K., Giamarelou, M., Bossioli, E., Tombrou, M., Mihalopoulos, N., Eleftheriadis, K., Kalogiros, J., Allan, D.J., Bacak, A., Percival, C. J., Coe, H., Biskos, G., 2013. Chemical composition and hygroscopic properties of aerosol particles over the Aegean Sea. Atmos. Chem. Phys. 13, 11595–11608. https://doi.org/10.5194/acp-13-11595-2013.

Bond, T.C., Bergstrom, R.W., 2006. Light absorption by carbonaceous particles: an investigative review. Aerosol Sci. Technol. 40, 27–67. https://doi.org/10.1080/02786820500421521.

Bossioli, E., Tombrou, M., Kalogiros, J., Allan, J., Bacak, A., Bezantakos, S., Biskos, G., Coe, H., Jones, B.T., Kouvarakis, G., Mihalopoulos, N., Persival, C.J., 2016. Atmospheric composition in the eastern mediterranean: influence of biomass burning during summertime using the WRF-chem model. Atmos. Environ. 132, 317–331. https://doi.org/10.1016/j.atmosenv.2016.03.011.

Boucher, O., Randall, D., Artaxo, P., Bretherton, C., Feingold, G., Forster, P., Kerminen, V.-M., Kondo, Y., Liao, H., Lohmann, U., Rasch, P., Satheesh, S.K., Sherwood, S., Stevens, B., Zhang, X.Y., 2013. Clouds and aerosols. In: Stocker, T.F., Qin, D., Plattner, G.-K., Tignor, M., Allen, S.K., Doschung, J., Nauels, A., Xia, Y., Bex, V., andMidgley, P.M. (Eds.), Climate Change 2013: the Physical Science Basis, Contribution of Working Group I to the Fifth Assessment Report of the Intergovernmental Panel on Climate Change. CambridgeUniversityPress, Cambridge, UK and New York, NY, USA.

Bougiatioti, A., Fountoukis, C., Kalivitis, N., Pandis, S.N., Nenes, A., Mihalopoulos, N., 2009. Cloud condensation nuclei measurements in the marine boundary layer of the Eastern Mediterranean: CCN closure and droplet growth kinetics. Atmos. Chem. Phys. 9, 7053–7066. https://doi.org/10.5194/acp-9-7053-2009.

Bougiatioti, A., Bezantakos, S., Stavroulas, I., Kalivitis, N., Kokkalis, P., Biskos, G., Mihalopoulos, N., Papayannis, A., Nenes, A., 2016. Biomass-burning impact on CCN number, hygroscopicity and cloud formation during summertime in the eastern Mediterranean. Atmos. Chem. Phys. 16, 7389–7409. https://doi.org/10.5194/acp-16-7389-2016.

Charlson, R.J., Schwartz, S.E., Hales, J.M., Cess, R.D., Coakley Jr., J.A., Hansen, J.E., Hofmann, D.J., 1992. Climate forcing by anthropogenic aerosols. Science 255, 423–430. https://doi.org/10.1126/science.255.5043.423.

Coakley Jr., J.A., Cess, R.D., Yurevich, F.B., 1983. The effect of tropospheric aerosols on the earth's radiation budget: a parameterization for climate models. J. Atmos. Sci. 40, 116–138. https://doi.org/10.1175/1520-0469(1983)040<0116:TEOTAO>2.0.CO;2.

Dandou, A., Tombrou, M., Kalogiros, J., Bossioli, E., Biskos, G., Mihalopoulos, N., Coe, H., 2017. Investigation of turbulence parametrization schemes with reference to the atmospheric boundary layer over the Aegean Sea during etesian winds. Boundary-Layer Meteorol. 164, 303–329. https://doi.org/10.1007/s10546-017-0255-0.

Dayan, U., Heffter, J., Miller, J., Gutman, G., 1991. Dust intrusionevents into the Mediterranean basin. J. Appl. Meteorol. 30, 1185–1199. https://doi.org/10.1175/1520-0450(1991)030<1185:DIEITM>2.0.CO;2.

Di Biagio, C., Di Sarra, A., Meloni, D., Monteleone, F., Piacentino, S., Sferlazzo, D., 2009. Measurements of mediterranean aerosol radiative forcing and influence of the single scattering albedo. J. Geophys. Res. Atmos. 114 (6) https://doi.org/10.1029/2008JD011037.

Emery, C., Liu, Z., Russell, A.G., Odman, M.T., Yarwood, G., Kumar, N., 2017. Recommendations on statistics and benchmarks to assess photochemical model performance. J. Air Waste Manage. 67, 582–598. https://doi.org/10.1080/10962247.2016.1265027.

Fast, J.D., Gustafson Jr., W.I., Easter, R.C., Zaveri, R.A., Barnard, J.C., Chapman, E.G., Grell, G.A., 2006. Evolution of ozone, particulates, and aerosol direct forcing in an urban area using a new fully-coupled meteorology, chemistry, and aerosol model. J. Geophys. Res. 111, D21305. https://doi.org/10.1029/2005JD006721.

Ferrero, L., Močnik, G., Cogliati, S., Gregorič, A., Colombo, R., Bolzacchini, E., 2018. Heating rate of light absorbing aerosols: time-resolved measurements, the role of clouds, and source identification. Environ. Sci. Technol. 52 (6), 3546–3555. https://doi.org/10.1021/acs.est.7b04320.

Flaounas, E., Kotroni, V., Lagouvardos, K., Klose, M., Flamant, C., Giannaros, T.M., 2017. Sensitivity of the WRF-Chem (V3.6.1) model to different dust emission parametrisation: assessment in the broader Mediterranean region. Geosci. Model Dev. (GMD) 10, 2925–2945. https://doi.org/10.5194/gmd-10-2925-2017.

Georgiou, G.K., Christoudias, T., Proestos, Y., Kushta, J., Hadjinicolaou, P., Lelieveld, J., 2018. Air quality modelling in the summer over the eastern Mediterranean using WRF-Chem: chemistry and aerosol mechanism intercomparison. Atmos. Chem. Phys. 18, 1555–1571. https://doi.org/10.5194/acp-18-1555-2018.

Georgoulias, A.K., Kourtidis, K.A., Alexandri, G., Rapsomanikis, S., Sanchez-Lorenzo, A., 2015. Common summertime total cloud cover and aerosol optical depth weekly variabilities over Europe: sign of the aerosol indirect effects? Atmos. Res. 53, 59–73. https://doi.org/10.1016/j.atmosres.2014.07.031.

Gerber, H.E., 1979. Absorption of 632.8 nm radiation by maritime aerosols near Europe. J. Atmos. Sci. 36, 2502–2512. https://doi.org/10.1175/1520-0469(1979)036<2502:AONRBM>2.0.CO;2.

Gordon, H., Field, P.R., Abel, S.J., Dalvi, M., Grosvenor, D.P., Hill, A.A., Johnson, B.T., Miltenberger, A.K., Yoshioka, M., Carslaw, K.S., 2018. Large simulated radiative effects of smoke in the south-east Atlantic. Atmos. Chem. Phys. 18, 15261–15289. https://doi.org/10.5194/acp-18-15261-2018.

Guenther, A.B., Zimmerman, P.R., Harley, P.C., Monson, R.K., Fall, R.K., 1993. Isoprene and monoterpene emission rate variability: model evaluations and sensitivity analyses. J. Geophys. Res. Atmos. 98, 12609–12617. https://doi.org/10.1029/93JD00527.

Gunn, R., Phillips, B.B., 1957. An experimental investigation of the effect of air pollution on the initiation of rain. J. Meteorol. 14, 272–280. https://doi.org/10.1175/1520-0469(1957)014<0272:AEIOTE>2.0.CO;2.

Hansen, J., Sato, M., Ruedy, R., 1997. Radiative forcing and climate response. J. Geophys. Res. 102, 6831–6864. https://doi.org/10.1029/96JD03436.

Highwood, E.J., Haywood, J.M., Coe, H., Cook, J., Osborne, S.R., Williams, P.I., Crosier, J., Bower, K.N., Formenti, P., McQuaid, J., Brooks, B.J., Thomas, G.E., Grainger, R.G., Barnaba, F., Gobbi, P., de Leeuw, G., Hopkins, J., 2007. Aerosol direct radiative impact experiment (ADRIEX) overview. Q. J. Roy. Meteorol. Soc. 133 (Suppl. 1), 3–15. https://doi.org/10.1002/qj.89.

Iacono, M.J., Delamere, J.S., Mlawer, E.J., Shephard, M.W., Clough, S.A., Collins, W.D., 2008. Radiative forcing by long-lived greenhouse gases: calculations with the aer radiative transfer model. J. Geophys. Res. 113 https://doi.org/10.1029/2008JD009944. D13103-1609.

IPCC, 2013. Summary for policymakers. In: Stocker, T.F., Qin, D., Plattner, G.-K., Tignor, M., Allen, S.K., Boschung, J., Nauels, A., Xia, Y., Bex, V., Midgley, P.M. (Eds.), Climate Change 2013: the Physical Science Basis. Contribution of Working Group I to the Fifth Assessment Report of the Intergovernmental Panel on Climate Change. Cambridge University Press, Cambridge, United Kingdom and New York, NY, USA.

Jacobson, M.Z., 2002. Control of fossil-fuel particulate black carbon and organic matter, possibly the most effective method of slowing global warming. J. Geophys. Res. 107 (D19), 4410. https://doi.org/10.1029/2001JD001376.

Jacobson, M.Z., 2012. Investigating cloud absorption effects: global absorption properties of black carbon, tar balls, and soil dust in clouds and aerosols. J. Geophys. Res. 117, D06205. https://doi.org/10.1029/2011JD017218.

Jacobson, M.Z., 2014. Effects of biomass burning on climate, accounting for heat and moisture fluxes, black and brown carbon, and cloud absorption effects. J. Geophys. Res. Atmos. 119, 8980–9002. https://doi.org/10.1002/2014JD021861.

Jin, Q., Yang, Z.-L., Wei, J., 2016. High sensitivity of Indian summer monsoon to Middle East dust absorptive properties. Sci. Rep. 6, 30690. https://doi.org/10.1038/srep30690.

Kosmopoulos, P.G., Kazadzis, S., Taylor, M., Athanasopoulou, E., Speyer, O., Raptis, P.I., Marinou, E., Proestakis, E., Solomos, S., Gerasopoulos, E., Amiridis, V., Bais, A., Kontoes, C., 2017. Dustimpact on surface solar irradiance assessed with model simula-tions, satellite observations and ground-based measurements. Atmos. Meas. Tech. 10, 2435–2453. https://doi.org/10.5194/amt-10-2435-2017.

Kushta, J., Kallos, G., Astitha, M., Solomos, S., Spyrou, C., Mitsakou, C., Lelieveld, J., 2014. Impact of natural aerosols on atmospheric radiation and consequent feedbacks with the meteorological and photochemical state of the atmosphere. J. Geophys. Res. 119 (3), 1463–1491. https://doi.org/10.1002/2013JD020714.

Lelieveld, J., Berresheim, H., Borrmann, S., Crutzen, P.J., Dentener, F.J., Fischer, H., Feichter, J., Flatau, P.J., He-land, J., Holzinger, R., Korrmann, R., Lawrence, M.G., Levin, Z., Markowicz, K.M., Mihalopoulos, N., Minikin, A., Ramanathan, V., de Reus, M., Roelofs, G.J., Scheeren, H.A., Sciare, J., Schlager, H., Schultz, M., Siegmund, P., Steil, B., Stephanou, E.G., Stier, P., Traub, M., Warneke, C., Williams, J., Ziereis, H., 2002. Global air pollution cross-roads over the Mediterranean. Science 298, 794–799. https://doi.org/10.1126/science.1075457.

Lundgren, K., Vogel, B., Vogel, H., Kottmeier, C., 2013. Direct radiative effects of sea salt for the Mediterranean region under conditions of low to moderate wind speeds. J. Geophys. Res. Atmos. 118, 1906–1923. https://doi.org/10.1029/2012JD018629.

Mallet, M., Dubovik, O., Nabat, P., Dulac, F., Kahn, R., Sciare, J., Paronis, D., Léon, J.F., 2013. Absorption properties of Mediterranean aerosols obtained from multi-year ground-based remote sensing observations. Atmos. Chem. Phys. 13, 9195–9210. https://doi.org/10.5194/acp-13-9195-2013.

Mallet, M., Dulac, F., Formenti, P., Nabat, P., Sciare, J., Roberts, G., Pelon, J., Ancellet, G., Tanré, D., Parol, F., Denjean, C., Brogniez, G., di Sarra, A., Alados-Arboledas, L., Arndt, J., Auriol, F., Blarel, L., Bourrianne, T., Chazette, P., Chevaillier, S., Claeys, M., D'Anna, B., Derimian, Y., Desboeufs, K., Di Iorio, T., Doussin, J.-F., Durand, P., Féron, A., Freney, E., Gaimoz, C., Goloub, P., Gómez-Amo, J.L., Granados-Muñoz, M.J., Grand, N., Hamonou, E., Jankowiak, I., Jeannot, M., Léon, J.-F., Maillé, M., Mailler, S., Meloni, D., Menut, L., Momboisse, G., Nicolas, J., Podvin, T., Pont, V., Rea, G., Renard, J.-B., Roblou, L., Schepanski, K., Schwarzenboeck, A., Sellegri, K., Sicard, M., Solmon, F., Somot, S., Torres, B., Totems, J., Triquet, S., Verdier, N., Verwaerde, C., Waquet, F., Wenger, J., Zapf, P., 2016. Overview of the chemistry-aerosol mediterranean experiment/aerosol direct radiative forcing on the mediterranean climate (ChArMEx/ADRIMED) summer 2013 campaign. Atmos. Chem. Phys. 16, 455–504. https://doi.org/10.5194/acp-16-455-2016.

Markowicz, K.M., Flatau, P.J., Ramana, W., Crutzen, P.J., Ramanathan, V., 2002. Absorbing mediterranean aerosols lead to a large reduction in the solar radiation at the surface. Geophys. Res. Lett. 29, 1968. https://doi.org/10.1029/2002GL015767.

McKeen, S.A., Hsie, E.Y., Trainer, M., Tallamraju, R., Liu, S.C., 1991. A regional model study of the ozone budget in the eastern United States. J. Geophys. Res. 96, 10809–10846.

Meloni, D., Junkermann, W., Di Sarra, A., Cacciani, M., De Silvestri, L., Di Iorio, T., Estellés, V., Gómez-Amo, J.L., Pace, G., Sferlazzo, D.M., 2015. Altitude-resolved shortwave and longwave radiative effects of desert dust in the Mediterranean during the GAMARF campaign: indications of a net daily cooling in the dust layer. J. Geophys. Res. Atmos. 120 (8), 3386–3407. https://doi.org/10.1002/2014JD022312.

Methymaki, G., Bossioli, E., Dandou, A., Kalogiros, J., Biskos, G., Mihalopoulos, N., Nenes, A., Tombrou, M., 2018. Solar irradiance prediction over the Aegean Sea: shortwave parameterization schemes and aerosol radiation feedback. In: Mensink, C., Kallos, G. (Eds.), Air Pollution Modeling and its Application XXV, ITM 2016. Springer International Publishing, Cham, Switzerland, pp. 141–145.

Mishra, A.K., Klingmueller, K., Fredj, E., Lelieveld, J., Rudich, Y., Koren, I., 2014. Radiative signature of absorbing aerosol over the eastern Mediterranean basin. Atmos. Chem. Phys. 14, 7213–7231. https://doi.org/10.5194/acp-14-7213-2014. https://search.crossref.org/?q=Radiative+signature+of+absorbing+aerosol+over+the+eastern+Mediterranean+basin.

Nabat, P., Somot, S., Mallet, M., Sanchez-Lorenzo, A., Wild, M., 2014. Contribution of anthropogenic sulfate aerosols to the changing Euro-Mediterranean climate since 1980. Geophys. Res. Lett. 41 (15), 5605–5611. https://doi.org/10.1002/2014GL060798.

Perrone, M.R., Bergamo, A., 2011. Direct radiative forcing during Sahara dust intrusions at a site in the Central Mediterranean: anthropogenic particle contribution. Atmos. Res. 101 (3), 783–798. https://doi.org/10.1016/j.atmosres.2011.05.011.

Pincus, R., Barker, H.W., Morcrette, J.-J.., 2003. A fast, flexible, approximate technique of computing radiative transfer for inhomogeneous clouds. J. Geophys. Res. 108, 4376. https://doi.org/10.1029/2002JD003322.

Qiu, Y., Liao, H., Zhang, R., Hu, J., 2017. Simulated impacts of direct radiative effects of scattering and absorbing aerosols on surface layer aerosol concentrations in China during a heavily polluted event in February 2014. J. Geophys. Res. Atmos. 122, 5955–5975. https://doi.org/10.1002/2016JD026309.

Ramanathan, V., Feng, Y., 2009. Air pollution, greenhouse gases and climate change: global and regional perspectives. Atmos. Environ. 43 (37–50).

Rao, S., Dey, S., 2020. Consistent signal of aerosol indirect and semi-direct effect on water clouds in the oceanic regions adjacent to the Indian subcontinent. Atmos. Res. 232, 104677. https://doi.org/10.1016/j.atmosres.2019.104677.

Roger, J., Mallet, M., Dubuisson, P., Cachier, H., Vermote, E., Dubovik, O., Despiau, S., 2006. A synergetic approach for estimating the local direct aerosol forcing: application to an urban zone during the Expérience sur Site pour Contraindre les Modèles de Pollution et de Transport d'Emission (ESCOMPTE) experiment. J. Geophys. Res. 111 (D13208), 13208–13216. https://doi.org/10.1029/2005JD006361.

Rosenfeld, D., 2000. Suppression of rain and snow by urban and industrial air pollution. Science 287, 1793–1796. https://doi.org/10.1126/science.287.5459.1793.

Saha, A., Mallet, M., Roger, J., Dubuisson, P., Piazzola, J., Despiau, S., 2008. One year measurements of aerosol optical properties over an urban coastal site: effect on local direct radiative forcing. Atmos. Res. 90, 195–202. https://doi.org/10.1016/j.atmosres.2008.02.003, 2008.

Schell, B., Ackermann, I.J., Hass, H., Binkowski, F.S., Ebel, A., 2001. Modeling the formation of secondary organic aerosol within a comprehensive air quality model system. J. Geophys. Res. Atmos. 106, 28275–28293. https://doi.org/10.1029/2001JD000384.

Sicard, M., Barragan, R., Dulac, F., Alados-Arboledas, L., Mallet, M., 2016. Aerosol optical, microphysical and radiative properties at regional background insular sites in the western Mediterranean. Atmos. Chem. Phys. 16, 12177–12203. https://doi.org/10.5194/acp-16-12177-2016.

Sofiev, M., Vankevich, R., Lotjonen, M., Prank, M., Petukhov, V., Ermakova, T., Koskinen, J., Kukkonen, J., 2009. An operational system for the assimilation of the satellite information on wild-land fires for the needs of air quality modelling and forecasting. Atmos. Chem. Phys. 9, 6833–6847. https://doi.org/10.5194/acp-9-6833-2009.

Spyrou, C., Kallos, G., Mitsakou, C., Athanasiadis, P., Kalogeri, C., Iacono, M.J., 2013. Modeling the radiative effects of desert dust on weather and regional climate. Atmos. Chem. Phys. 13, 5489–5504. https://doi.org/10.5194/acp-13-5489-2013.

Stock, M., Cheng, Y.F., Birmili, W., Massling, A., Wehner, B., Müller, T., Leinert, S., Kalivitis, N., Mihalopoulos, N., Wiedensohler, A., 2011. Hygroscopic properties of atmospheric aerosol particles over the Eastern Mediterranean: implications for regional direct radiative forcing under clean and polluted conditions. Atmos. Chem. Phys. 11, 4251–4271. https://doi.org/10.5194/acp-11-4251-2011.

Stockwell, W.R., Middleton, P., Chang, J.S., Tang, X., 1990. The second generation regional acid deposition model chemical mechanism for regional air quality modelling. J. Geophys. Res. Atmos. 95, 16343–16367. https://doi.org/10.1029/JD095iD10p16343.

Tombrou, M., Bossioli, E., Protonotariou, A.P., Flocas, H., Giannakopoulos, C., Dandou, A., 2009. Coupling GEOS-CHEM with a regional air pollution model for Greece. Atmos. Environ. 43, 4793–4804. https://doi.org/10.1016/j.atmosenv.2009.04.003.

Tombrou, M., Bossioli, E., Kalogiros, J., Allan, J.D., Bacak, A., Biskos, G., Coe, H., Dandou, A., Kouvarakis, G., Mihalopoulos, N., Percival, C.J., Protonotariou, A.P., Szabo-Takacs, B., 2015. Physical and chemical processes of air masses in theAegean Sea during Etesians: Aegean-GAME airborne campaign. Sci. Total Environ. 506–507, 201–216. https://doi.org/10.1016/j.scitotenv.2014.10.098.

Twomey, S.A., 1972. The effect of cloud scattering on the absorption of solar radiation by atmospheric dust. J. Atmos. Sci. 29, 1156–1159. https://doi.org/10.1175/1520-0469(1972)029<1156:TEOCSO>2.0.CO;2.

Twomey, S.A., 1974. Pollution and the planetary albedo. Atmos. Environ. 8, 1251–1256. https://doi.org/10.1016/0004-6981(74)90004-3.

Twomey, S.A., 1977. The influence of pollution on the shortwave albedo of clouds. J. Atmos. Sci. 34, 1149–1152. https://doi.org/10.1175/1520-0469(1977)034<1149:TIOPOT>2.0.CO;2.

Tyrlis, E., Lelieveld, J., 2013. Climatology and dynamics of the summer Etesian winds over the eastern Mediterranean. J. Atmos. Sci. 70, 3374–3396. https://doi.org/10.1175/JAS-D-13-035.1.

Valenzuela, A., Arola, A., Antón, M., Quirantes, A., Alados-Arboledas, L., 2017. Black carbon radiative forcing derived from AERONET measurements and models over an urban location in the southeastern Iberian Peninsula. Atmos. Res. 191, 44–56. https://doi.org/10.1016/j.atmosres.2017.03.007.

Wilcox, E.M., 2012. Direct and semi-direct radiative forcing of smoke aerosols over clouds. Atmos. Chem. Phys. 12, 139–149. https://doi.org/10.5194/acp-12-139-2012.

Yao, H., Song, Y., Liu, M., Archer-Nicholls, S., Lowe, D., McFiggans, G., Xu, T., Du, P., Li, J., Wu, Y., Hu, M., Zhao, C., Zhu, T., 2017. Direct radiative effect of carbonaceous aerosols from crop residue burning during the summer harvest season in East China. Atmos. Chem. Phys. 17, 5205–5219. https://doi.org/10.5194/acp-17-5205-2017.

Zanatta, M., Gysel, M., Bukowiecki, N., Müller, T., Weingartner, E., Areskoug, H., Fiebig, M., Yttri, K.E., Mihalopoulos, N., Kouvarakis, G., Beddows, D., Harrison, R. M., Cavalli, F., Putaud, J.P., Spindler, G., Wiedensohler, A., Alastuey, A., Pandolfi, M., Sellegri, K., Swietlicki, E., Jaffrezo, J.L., Baltensperger, U., Laj, P., 2016. A European aerosol phenomenology-5: climatology of black 1058 carbon optical properties at 9 regional background sites across Europe. Atmos. Environ. 145, 346–364. https://doi.org/10.1016/j.atmosenv.2016.09.035.

Zempila, M.M., Giannaros, T.M., Bais, A., Melas, D., Kazantzidis, A., 2016. Evaluation of WRF shortwave radiation parameterizations in predicting Global Horizontal Irradiance in Greece. Renew. Energy 86, 831–840. https://doi.org/10.1016/j.renene.2015.08.057.

Zhou, Y., Savijärvi, H., 2014. The effect of aerosols on long wave radiation and global warming. Atmos. Res. 135–136, 102–111. https://doi.org/10.1016/j.atmosres.2013.08.009.

Zhou, X., Ackerman, A.S., Fridlind, A.M., Wood, R., Kollias, P., 2017. Impacts of solar-absorbing aerosol layers on the transition of stratocumulus to trade cumulus clouds. Atmos. Chem. Phys. 17, 12725–12742. https://doi.org/10.5194/acp-17-12725-2017.